ELSEVIER

Journal of Electroanalytical Chemistry 500 (2001) 418–434

Journal of Electroanalytical Chemistry

www.elsevier.nl/locate/jelechem

Adsorption of bromide at the Ag(100) electrode surface

Th. Wandlowski [a,*], J.X. Wang [b], B.M. Ocko [c]

[a] *Institut für Grenzflächenforschung und Vakuumphysik, Forschungszentrum Jülich GmbH, D-52425 Jülich, Germany*
[b] *Department of Applied Science, Brookhaven National Laboratory, Upton, NY 11790, USA*
[c] *Department of Physics, Brookhaven National Laboratory, Upton, NY 11790, USA*

Received 11 July 2000; received in revised form 12 August 2000; accepted 22 August 2000

In honor of Professor R. Parsons on the occasion of his retirement as the Editor of the Journal of Electroanalytical Chemistry

Abstract

The adsorption and phase formation of bromide on Ag(100) has been studied by chronocoulometry and surface X-ray scattering (SXS). With increasing electrode potential, bromide undergoes a phase transition from a lattice gas to an ordered c(2×2) structure ($\theta = 0.5$). The degree of lateral disorder was estimated by comparing the SXS- and the electrochemical measurements. Based on chronocoulometric experiments, a thermodynamic analysis of charge density data was performed to describe the bromide adsorption at the Ag(100) electrode. The Gibbs surfaces excess, electrosorption valencies, Esin–Markov coefficients, and the Gibbs energy of adsorption, lateral interaction energies as well as surface dipole moments have been estimated. The experimental θ versus E- isotherms are modeled employing (i) a quasi-chemical approximation as well as (ii) the results of a recent Monte Carlo simulation. An attempt is made to discuss the structure data and thermodynamic quantities of bromide adsorption on Ag(100) on the basis of the Grahame–Parsons model of the Helmholtz layer. © 2001 Elsevier Science B.V. All rights reserved.

Keywords: Bromide adsorption; Ag(100) electrodes; Chronocoulometry

1. Introduction

Ionic adsorption at metal electrodes is one of the most fundamental questions of interfacial electrochemistry. Historically most experimental and theoretical work was confined to the mercury or polycrystalline solid electrode | electrolyte interfaces [1–3]. Important advances in understanding the properties and structures of metal | electrolyte interfaces emerged with the availability of well-defined single crystals as substrate materials, such as Au(*hkl*), Ag(*hkl*) or Pt(*hkl*) [4,5]. Here thermodynamic and kinetic methods e.g. capacitance measurements, cyclic voltammetry or chronocoulometry are still applicable to characterise the interfacial behaviour of ions on these electrodes qualitatively [4,5], or, if desirable, to quantify the energetics and dynamics of adsorption [7–11]. These classical electrochemical studies provide a macroscopic description of adsorption and/or phase formation processes but lack direct structural information. This missing information may be obtained from spectroscopic techniques like electroreflectance [12], infrared- or Raman-spectroscopy [13,14], second harmonic generation [15,16], or the use of UHV-techniques after emersion of the electrode [17]. As was shown recently, scanning probe microscopies [18,19] as well as surface X-ray scattering (SXS) methods [20,21] increase even further our abilities to monitor and understand the electrochemical interface at an atomistic level.

In this communication we will focus on interfacial properties of bromide ions adsorbed in-situ at the Ag(100) surface. Most quantitative adsorption studies of halide ions on silver single crystals have so far been confined to the (111) and (110) planes [6,22–28], exceptions are Refs. [6,23,27,28]. There, the adsorption of chloride [6], fluoride [23] and bromide [27,28] ions was investigated at Ag(100), using the method of mixed solutions with sodium fluoride or sodium hexafluorophosphate as the base electrolyte. At a qualita-

---

* Corresponding author. Fax: 49-2461-3907.
E-mail address: th.wandlowski@fz-juelich.de (Th. Wandlowski).

PII: S0022-0728(00)00380-6

tive level the interfacial behaviour of bromide at real and quasi-perfect (e.g. grown electrolytically in a teflon capillary) Ag(100) surfaces was previously investigated by means of differential capacity [6,29,30], electroreflectance [12], second harmonic generation [31] and measurements of the surface resistance [32]. Recent surface X-ray diffraction studies pointed to an order/disorder phase transition within the ionic adlayer [33]. Below the critical potential bromide is adsorbed at hollow sites but does not exhibit long-range order. At the critical potential new diffraction features emerge corresponding to the formation of an ordered c(2 × 2) structure with a correlation length extending to thousands of Å. The simplicity of this system presents a unique opportunity to study phase transitions in two-dimensions, models of isotherms, and models of the electrochemical double layer. These results have already motivated two different groups to carry out numerical simulations [35–37].

The objectives of the present article are twofold: we will discuss first the phase behaviour of bromide ions on a chemically etched and flame-annealed Ag(100) electrode based on capacitance and surface X-ray diffraction measurements. In the next section we will provide a comprehensive thermodynamic analysis of chronocoulometrically acquired charge density and surface excess data. We will analyse the energetics of adsorption in the low and finite coverage limits, and provide thermodynamic data such as adsorption isotherms, Gibbs energies of adsorption and electrosorption valencies. The nature of lateral interactions between bromide and the experimentally determined surface dipole moment formed between bromide ions and their image charge on the metal will be discussed. These macroscopic data are complemented with structural properties of the bromide adlayer as obtained in a series of in-situ surface X-ray scattering experiments. The comparison of results from both experimental approaches enables us to develop a rather detailed understanding of bromide adsorption on Ag(100).

2. Experimental

The electrochemical measurements were performed with Ag(100) single crystal electrodes (4 mm diameter, and 4 mm thickness) using the so-called hanging meniscus technique [38]. Silver disc electrodes (8 mm diameter, 2 mm thickness) were used in the X-ray measurements. The silver electrodes were chemically etched in cyanide solution before each experiment until the surface appeared shiny [39], and after careful rinsing in Milli-Q water®, annealed in a hydrogen flame for about 30 s. After cooling in a stream of dry nitrogen or argon the electrode was quickly transferred into the electrochemical or X-ray cell. Contact with the electrolyte was established under strict potential control, usually at values close to the potential of zero charge. We note that in-situ STM-experiments showed that the electrode preparation, as just described, generates large, atomically smooth terraces, hundreds of Å wide and separated by mono- and diatomic steps [40].

The solutions were prepared from Milli-Q®-water, $KClO_4$ (Fluka, puriss. p.a., twice recrystallized) and KBr (Merck, suprapure). $KClO_4$ was chosen as supporting electrolyte because it is (i) only weakly specifically adsorbed on Ag(100) [23] and (ii) can be prepared with very high purity. The latter is extremely difficult to achieve with KPF_6, and glass corrosion prevents the use of KF in long-term experiments. We note that one complete set of chronocoulometric data takes about 48 h. All solutions were thoroughly deaerated with 5N nitrogen prior to each experiment. Nitrogen was passed over the electrolyte in case of the electrochemical experiments or through the outer chamber of the X-ray cell. The counter electrode was a platinum wire, and a saturated calomel electrode (SCE) or a $Ag|AgCl|KCl_{sat}$ electrode in a side compartment served as reference. All potentials are quoted with respect to the SCE. The temperature was (20 ± 1)°C.

The set-up and procedures for the electrochemical experiments (cyclic voltammetry, capacitance measurements, chronocoulometry) were described previously [41]. We focus here only on some additional details of the chronocoulometric experiments: The potential was initially held at a value E_i between -1.375 and -0.400 V, up to 300 s for the lowest bromide concentrations, and then stepped to the final potential $E_f = -1.400$ V, where bromide is completely desorbed from the electrode surface. The waiting time at E_i was chosen (in control experiments) to be always sufficient to establish adsorption equilibrium. The first waiting potential was $E_i = -1.375$ V, and the current transient following a single potential step from $E_i = -1.375$ V to $E_f = -1.400$ V was subsequently recorded (usually 80 ms). Then the potential was stepped back to a new initial value E_i, 25 mV more positive than the previous one, and the cycle started once again until the last transient of each concentration ($E_i = -0.400$ to $E_f = -1.400$ V) was obtained. The current transients were digitally integrated to obtain the corresponding charge transients, which display an initial rising section and a well-developed plateau region. A slight increase in charge with time is observed only for the highest bromide concentrations and is attributed to an additional contribution, which is related to the onset of hydrogen reduction. The relative charge $\Delta q^M(t=0) = q^M(E_i) - q^M(E_f = -1.400\text{ V})$, consumed exclusively in the complete desorption of bromide ions, was obtained by linear extrapolation of the plateau region to zero time. This procedure was performed for the supporting electrolyte and for fifteen concentrations of $(0.05 - x)$ M $KClO_4 + x$ M KBr. The absolute charge densities q^M

were then calculated with the potential of zero charge of the base electrolyte, $E_{pzc} \approx -0.885$ V, obtained in capacitance experiments, and after normalisation with the electrode area $A = 0.125$ cm^2. The value of E_{pzc} is in good agreement with previously reported data for Ag(100) in 0.05 M $KClO_4$ [42].

The X-ray experiments were carried out with focussed monochromatic radiation, $\lambda = 1.20$ Å ($\lambda = 1.54$ Å), at the beam line X22A (X22B) of the National Synchrotron Light Source at Brookhaven National Laboratory. The scattering vector (H, K, L) is expressed in terms of a body-centred tetragonal (primitive) unit cell [33,34]. The atomic positions can be described by the basis vectors a, b, in plane, and by c along the surface normal, where $|a| = |b| = 2.889$ Å and $|c| = \sqrt{2}\ a_{nn} = 4.086$ Å, $a_{nn} = 2.889$ Å is the silver nearest neighbour separation. The corresponding reciprocal space basis is given by (a^*, b^*, c^*) (H, K, L), where $|a^*| = |b^*| = 2\pi/a_{nn} = 2.175$ Å^{-1} and $|c^*| = 2\pi/\sqrt{2}\ a_{nn} = 1.538$ Å^{-1}. The in-plane diffraction experiments were carried out in the (H, K)-plane with L typically 0.12, corresponding to a grazing incidence angle of 1.1°. For further details of the SXS-experiments we refer to Refs. [33,34].

3. Results and discussion

3.1. Phase behaviour

3.1.1. Capacitance measurements

Fig. 1(A) shows a set of four capacitance curves recorded for the Ag(100) electrode in $(0.05 - x)$ M $KClO_4 + x$ M KBr after continuous cycling between $-1.500 \leq E \leq -0.300$ V, scan rate 10 mV s^{-1}. All curves merge with the capacitance curve of the base electrolyte (dotted line) at potentials negative of -1.400 V, which indicates complete desorption of the halide ions. The adsorption of bromide ions at less negative potentials is characterised by a substantial, and apparently concentration-dependent increase of the interfacial capacitance, which also gives rise to a broad feature P1. The latter is followed by a second, but rather sharp peak labelled P2. The capacitance drops abruptly and reaches its saturation value of 17 μF cm^{-2} at $E \geq -0.400$ V and at bromide concentrations $c(Br^-)$ larger than 10^{-3} M. Valette et al. [6] suggested for the case of chloride adsorption on the low-index faces of Ag(hkl) that a maximum rather similar to P1 is most probably associated with water reorientation in the Helmholtz-layer.

There is significant hysteresis between the positive and the corresponding negative going scans of the capacitance for $c(Br^-) < 10^{-3}$ M, as indicated by curve 2 in Fig. 1(A). This is probably due to mass transport and/or a slow adsorption/phase formation process [43–45]. These data demonstrate that capacitance measurements at conditions as presented in Fig. 1 (18 Hz, ac-frequency, 10 mV peak-to-peak amplitude, sweep rate 10 mV s^{-1}) do not provide equilibrium data for bromide adsorption in the low and medium concentration regions, and are therefore not adequate for the determination of any thermodynamic quantities. Nevertheless, we would like to mention that the positions of both maxima shift linearly towards negative potentials with increasing bromide concentration. The slope, $\partial E/\partial \ln c = (-0.070 \pm 0.008)$ mV, was estimated from the negative going scans.

3.1.2. In-situ surface X-ray diffraction studies

The scattering from a crystalline surface differs from that of an ideal bulk sample. Whereas the latter gives rise to three-dimensional Bragg peaks, the former gives rise to rods of scattering which are oriented along the surface normal direction [46]. These rods satisfy the Bragg condition within the surface plane and are extended in the third direction. For a well terminated Ag(100) surface, rods of scattering occur at all (H, K) integer positions (tetragonal co-ordinates) and true Bragg peaks occur at integer (H, K, L) when $H + K + L$ is even. The analysis of the in-plane X-ray scattering profiles in the presence of bromide yields an average lower bound of the coherence length of 3500 Å, which represents the terrace size. These results clearly indicate the existence of a stable and well-ordered Ag(100)$-(1 \times 1)$ substrate surface in our experiments [33,34,47].

At potentials less than P2, only the integer (H, K) rods were observed and the absence of additional spots indicates that the adsorbed bromide did not exhibit long-range order. On the other hand, at potentials positive of P2 new diffraction spots developed at half order positions. Four independent reflections at (1/2, 1/2), (1/2, 3/2), (1/2, 5/2) and (3/2, 3/2) as well as their corresponding symmetry equivalents were found. This diffraction pattern corresponds to a square c(2 × 2) adlayer structure and is illustrated in Fig. 1(C). The same diffraction pattern was reported in a LEED study by Taylor et al. [48] for bromide adsorbed on the vacuum/Ag(100) surface. For this square structure, the bromide–bromide separation is 4.086 Å, and the coverage, θ_x, normalised with respect to the underlying substrate lattice is 0.5. Within the c(2 × 2) phase the X-ray scattering profiles are almost resolution limited and the excess width gives a correlation length (terrace size) of 3000 Å [33,34,47].

A comparison of the potential-dependent X-ray and capacitance measurements (on the same potential scales) provides further proof that the peak in the capacitance, P2, occurs at the order–disorder transition (see Fig. 1(A and B). In Fig. 1(B) the intensity of the peak at (1/2, 1/2, 0.12) is shown (after subtracting the diffuse background) for the 0.04 M KBr + 0.01 M

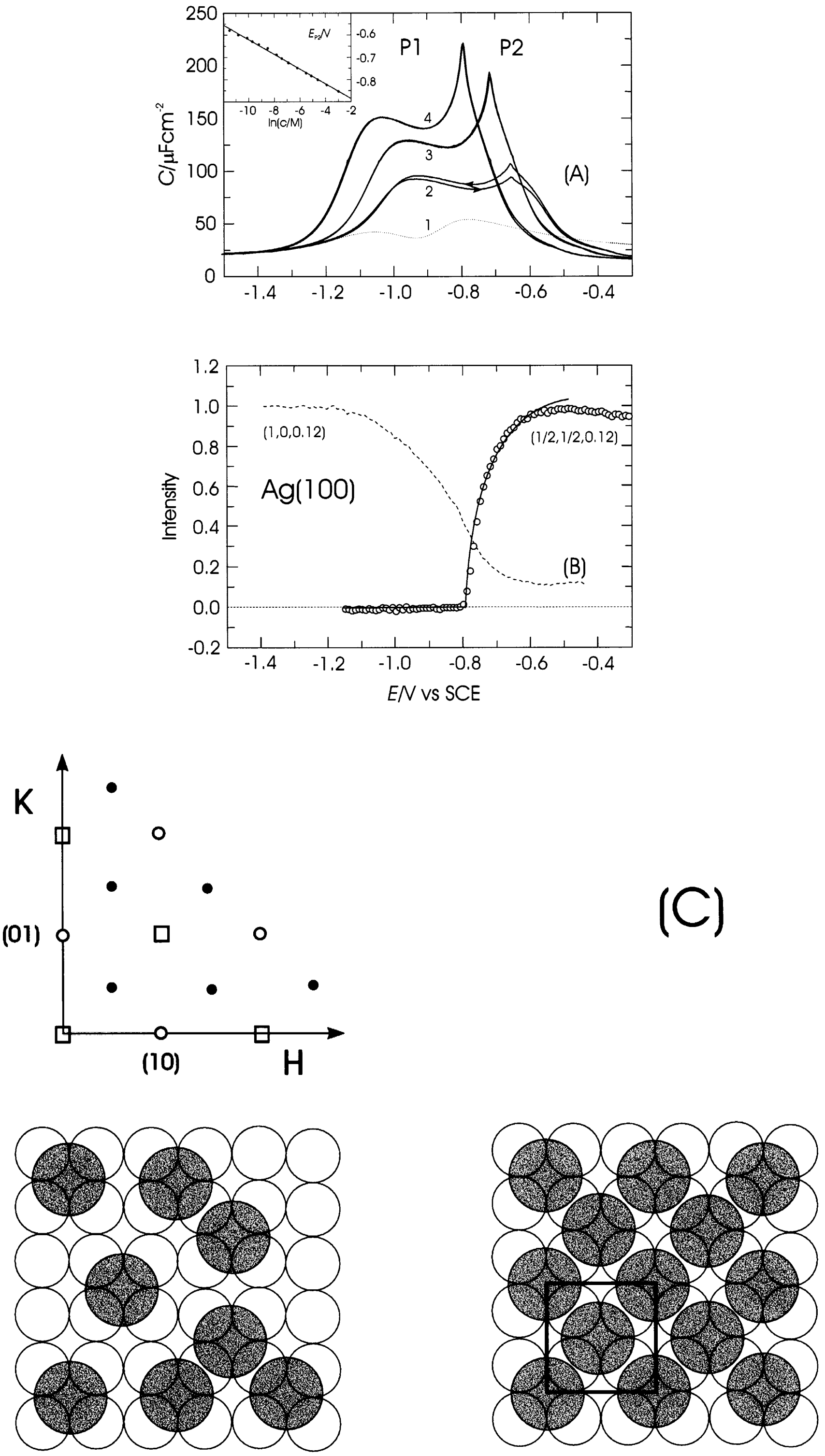

Fig. 1. (A) Capitance versus potential curves for Ag(100) in $(0.05 - x)$ M $KClO_4 + x$ M KBr; x represents the KBr concentrations: (1) – 0, (2) – 2 10^{-4} M, (3) – 10^{-3} M, (4) – 10^{-2} M. Scan rate 10 mV s^{-1}, 18 Hz and 10 mV peak-to-peak ac-amplitude. The inset shows the concentration dependence of the positive sharp maximum P2. (B) Potential dependence of the normalised scattering intensity of Ag(100) in 0.04 M $KClO_4$ + 0.01 M KBr at (1/2, 1/2, 0.12) (○, reflection of the c(2 × 2) adlayer) and at (1, 0, 0.12) (dashed line, Ag(100) – (1 × 1) surface rod). Power-law fits to the (1/2, 1/2, 0.12)-signal are shown with the exponent 0.125 as solid line. (C) In-plane diffraction pattern of the commensurate $c(2 \times 2)$ bromide adlayer structure as obtained at 0.500 V (top). The open circles represent Bragg rods, the open squares Bragg peaks. The measured bromide superstructure reflections are indicated by the solid circles. The real space structures of the lattice-gas configuration (left) and the commensurate c(2 × 2) bromide adlayer (right) are also shown.

$KClO_4$ solution. The initial rise in the intensity at approximately -0.80 V is well correlated with the peak P2 observed in the capacitance curve (Fig. 1(A)). The intensity continues to increase as the potential is raised and eventually saturates at about -0.50 V. The saturation suggests that a well-ordered $c(2 \times 2)$ adlayer exists. The lack of further adsorption at potentials above -0.5 V is also supported by the small background level of the capacitance.

On the basis of X-ray and the chronocoulometry measurements (reported below) the bromide coverage appears to change continuously over the entire potential region and there is no indication of a step in coverage. The continuous coverage change indicates that the order–disorder transition is second order. This order–disorder transition is isomorphic to the two-dimensional Ising transition where the coverage is analogous to the staggered magnetisation order parameter [33,34]. The intensity at (1/2, 1/2) is proportional to the order parameter squared and should follow a power-law, i.e. $(E - E_c)^{-2\beta}$ for $E > E_c$. The Ising exponent, $\beta = 0.125$, provides a good description of the critical behaviour up to 80% of the saturation intensity (Fig. 1(B), solid line). Clearly, the mean field prediction $\beta = 0.5$ [49] does not represent the observed critical behaviour.

Further information on the nature of the bromide adsorption, especially at potentials negative of P2, is revealed by the potential dependent X-ray intensity at (1, 0, L) positions. Here, the scattered intensity is sensitive to both the arrangement of the adsorbate layer and of the surface silver atoms. The onset of the slow decrease of the (1, 0, 0.12) intensity with increasing electrode potential correlates with the appearance of the broad feature P1 in the capacitance curve (cf. curve 4 in Fig. 1(A) and dashed line in Fig. 1(B)). No discontinuity is observed around P2. At the most positive potentials, where the ordered $c(2 \times 2)$ adlayer is developed, the (1, 0, 0.12) intensity levels off and approaches 0.12, obtained after background subtraction and normalisation to its maximum around -1.300 V in the absence of adsorbed bromide. This result demonstrates that a significant percentage of the bromide scattering amplitude within the disordered region is out-of-phase with that of the substrate. This out-of-phase condition occurs when the bromide ions are adsorbed in the fourfold hollow sites of the substrate. Adsorption on a-top sites would give rise to an increase of the (1, 0, 0.12) intensity with increasing coverage [46,47]. On this basis we conclude that the disordered phase represents a lattice gas with the bromide ions preferentially localised in fourfold hollow sites. The potential-dependent coverage, assuming adsorption in perfectly fourfold hollow sites was calculated from the quantitative analysis of the X-ray scattering intensity at (1, 0, 0.12) [33,34] and will be compared in Section 3.2 with the chronocoulometrically determined isotherms, which represent the overall amount of adsorbed bromide ions.

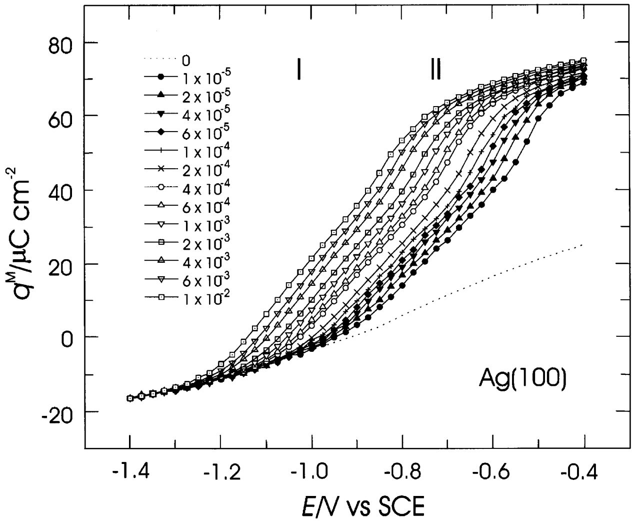

Fig. 2. Charge density versus electrode potential curves for Ag(100) in $(0.05 - x)$ M $KClO_4 + x$ M KBr, x (in M) as indicated in the figure.

Additional insight into the nature of the broad prewave P1 at low bromide coverages was obtained in a recent Monte Carlo study by Michell et al. [50]. Based on our X-ray scattering and preliminary electrochemical experiments [33,34,47] these authors argued that P1 might be caused by configurational fluctuations or short-range correlations in the disordered phase, which locally resemble other ordered phases with coverages of 0.25, such as $p(2 \times 2)$ and/or $c(4 \times 2)$, which are not stable at r.t. The interactions with surface water, as originally discussed by Valette et al. [6] seem to be of minor importance [35,50].

In conclusion, we have shown in this section that bromide adsorbs on Ag(100) at low coverages as a lattice gas, and with increasing coverage, following a continuous order–disorder phase transition, a highly uniform $c(2 \times 2)$ adlayer is formed. The results of our SXS-experiments are supported by a recent NEXAFS-study (near-edge X-ray adsorption fine structure) of Endo et al. [51].

3.2. Chronocoulometric measurements

3.2.1. Equilibrium charge density

Equilibrium data on the adsorption of bromide ions at Ag(100) electrodes was obtained from chronocoulometric measurements in a gently stirred solution. Fig. 2 shows a set of charge density curves for thirteen concentrations of KBr in $(0.05 - x)$ M $KClO_4 + x$ M KBr. These data are the direct experimental results which will be analysed in the following sections to extract thermodynamic quantities.

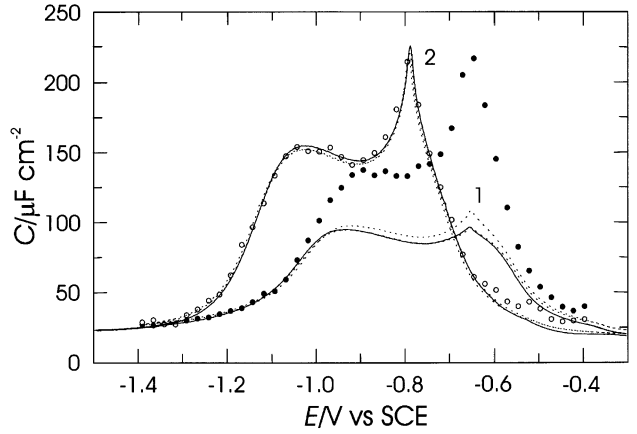

Fig. 3. Differential capacity curves of Ag(100) in 2×10^{-4} M KBr + 0.0498 M $KClO_4$ (1) and 0.01 M KBr + 0.04 M $KClO_4$ (2) determined as follows: (I) ac-impedance measurements (18 Hz and 10 mV peak-to-peak ac-amplitude). The full (dotted) lines represent scans of the electrode potential in the positive (negative) direction. Other conditions as in Fig. 1(A). (II) differentiation of the chronocoulometrically obtained charge density versus potential curves (open and filled circles).

Adsorption of bromide causes a positive charge to flow to the metal side of the interface. This also causes a negative shift of the potential of zero charge. Phenomenologically, the charge density versus potential curves as measured in the presence of bromide, are composed of two segments. The region of low charge densities (I) corresponds to the potential range of the broad feature in the capacitance curves. The second one appears just at a potential positive of the adlayer phase transition at P2 corresponding to charge densities between 43 and 50 μC cm^{-2}. It is characterised by an initial increase of $\partial q^{M}/\partial E$; subsequently the slope decreases and seems to become less dependent on the bromide concentration at the most positive potentials studied.

The above distinction is somewhat more emphasised by calculating the first derivatives of the experimental charge density curves with respect to potential. The results represent the thermodynamically well-behaved dc-equilibrium capacity. As exemplified in Fig. 3 for 0.04 M $KClO_4$ + 0.01 M KBr, the latter and the corresponding directly measured single-frequency ac-capacitance curves practically coincide at bromide concentrations larger than 1 mM within the entire potential region studied. Deviations between the two data sets at the most positive potentials might be associated with the flow of a small faradaic charge due to electro-oxidation of a submonolayer of silver oxide, which could be formed during the waiting time at E_i, as is explained in Ref. [42]. At lower bromide concentrations quantitative correlations do not exist (cf. 0.02 mM KBr solution). Here, the ac-capacity is systematically lower, especially around P1 and P2, which clearly indicates its non-equilibrium character (primarily due to mass-transport limitations), and hence this quantity is not suitable for any further thermodynamic analysis (cf. discussion in Refs. [43,44]).

3.2.2. Gibbs surface excess

The adsorption of bromide at the Ag(100) electrode was studied at constant ionic strength and in the presence of an excess of a rather inert supporting electrolyte. Assuming that the contribution of the surface stress does not significantly alter the change of the interfacial energy as a function of the electrode potential and adsorbate activity [52–56], the electrocapillary equation of the above system is given by

$$d\gamma = -q^{M}dE - \Gamma_c RT d\ln c_{Br} \quad (1)$$

where γ is the interfacial tension, and Γ_c is the Gibbs excess of bromide ions. For a detailed account of the validity of Eq. (1) to determine reasonably accurate values of the Gibbs surface excess in view of a criticism by Heiss and Sass [57] and Ibach et al. [58,59] we refer to our recent publication [60].

The excess of supporting electrolyte helps to ensure that Γ_c primarily represents the Gibbs excess in the Helmholtz layer, while its diffuse layer contribution is negligible. The Gibbs excess has been calculated at constant potential (Fig. 4(A)) and at constant surface charge (Fig. 4(B)) using the approach of Stolberg and Lipkowski [61]. In the first case, the film pressure $\pi(E) = (\gamma_o - \gamma)_E$ was calculated by integrating the charge density curves (see Fig. 2) in the base electrolyte (γ_o) and in the presence of the adsorbate (γ). The surface excess, shown in Fig. 4(A), was then obtained by the differential of $\pi(E)$ with respect to ln c_{Br}. Over a large range the coverage appears to increase linearly with potential. A finer examination shows a slight, but distinct increase in slope at a coverage of about 6.6×10^{-10} mol cm^{-2} close to the potential P2 of the order–disorder transition. At the most positive potentials the surface excess levels off and seems to approach a concentration-independent limit of $\Gamma_{cm} = 9.6 \times 10^{-10}$ mol cm^{-2}, which is equivalent to 5.78×10^{14} ions cm^{-2}. We use the subscript c to refer to the chronocoulometric data. To obtain Γ_c at constant charge the Parsons function $\xi = q^{M}E + \gamma$ was calculated. The surface excess, shown in Fig. 4(B), is then obtained by the differential of $\Phi = (\xi_o - \xi)_{q^M}$ with respect to ln c_{Br^-}.

We now compare the chronocoulometrically determined surface excess with results obtained in the X-ray scattering experiments. At $E > -0.60$ V a complete c(2 × 2) bromide adlayer is formed. The chronocoulometric result, $\Gamma_{cm} = 9.6 \times 10^{-10}$ mol cm^{-2}, is slightly smaller than the coverage $\Gamma_{xm} = 5.99 \times 10^{14}$ ions cm^{-2} (9.94×10^{-10} mol cm^{-2}) expected for a complete c(2 × 2) bromide adlayer. This small discrepancy (3.5%) may result from an error in the effective crystal area.

An independent measure of the coverage was also ascertained by using an X-ray interference scattering technique [33,34] which ascribes the intensity at (1, 0, 0.12) to adsorption in four-fold sites. The decrease in the scattering intensity to 11% of its level in the absence of bromide is exactly the value expected for half a monolayer (5.99×10^{14} ions cm^{-2}). The agreement between the three measures of the coverage in the saturation range, the electrochemical and two independently determined X-ray values, increases our confidence in the chronocoulometric results within the entire potential range.

In Fig. 5 we compare the normalised coverage results determined by chronocoulometry (θ_c) and X-ray (θ_x) measurements for 10 mM KBr in 40 mM $KClO_4$. Except at the highest potentials, the bromide coverage θ_x is smaller than θ_c. This discrepancy has its origin in the interference model used to extract the coverage, where it was assumed that all bromide ions are in exact four-fold sites. By relaxing this criteria, the ratio between the two coverages can be used to calculate an effective Gaussian type lateral rms bromide-displacement amplitude. This gives rise to a Debye–Waller-like term, where the displacement is estimated to be 0.9 Å at the most negative potentials and decreases to nearly zero at the highest coverages. As also shown in Fig. 5, at the disorder–order transition we find $\theta_x = 0.25$ and $\theta_c = 0.35$. The latter is close to the critical coverage of 0.368 obtained from simulations based on lattice gas adsorption with a pure hard square model [62,63].

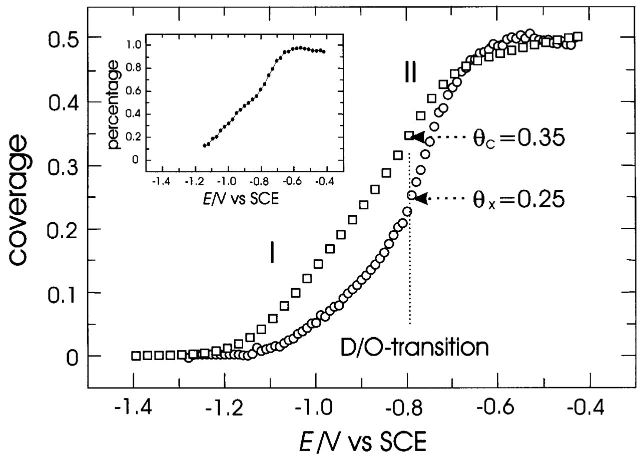

Fig. 5. Potential dependence of the normalised bromide coverage obtained chronocoulometrically (□) or by analysing the scattering intensity in the (1, 0, 0.1) position (○) for Ag(100) in 0.04 M $KClO_4$ + 0.01 M KBr. The inset shows the percentage of bromide ions, which resides in fourfold hollow-sites as a function of the electrode potential.

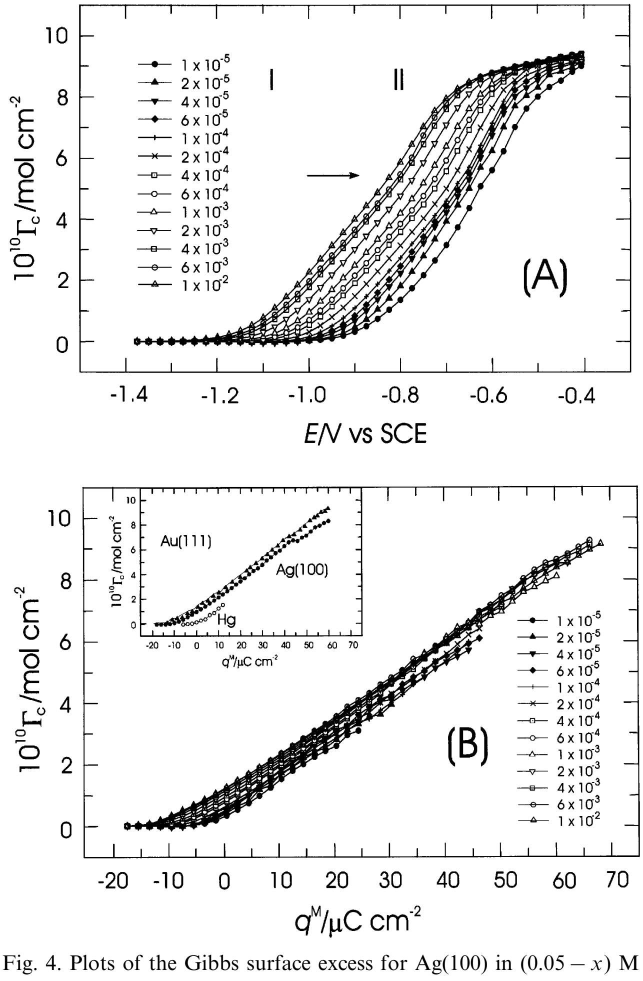

Fig. 4. Plots of the Gibbs surface excess for Ag(100) in $(0.05 - x)$ M $KClO_4 + x$ M KBr employing either the electrode potential (A) or the charge density (B) as the independent electrical variable. The inset of Fig. 4(B) shows Γ versus q^M curves in the presence of 10^{-3} Br for several systems: Ag(100)/0.049 M $KClO_4 + 10^{-3}$ M KBr (this work), Au(111)/0.1M $KClO_4 + 10^{-3}$ M KBr [65], and Hg/10^{-3} M NH_4Br + 1 M NH_4F [66].

The following picture emerges: at low bromide coverages the ions are more mobile, and they are not fully localised in the hollow sites, e.g. no long-range order exists at r.t. With increasing potential they become more localised. At the most positive potentials, where water is no longer coadsorbed and every other four-fold site is occupied, the adsorbate–adsorbate interactions are balanced and the bromides are situated exactly in the hollows with a very small excess lateral displacement.

When analysing the Gibbs excess Γ as a function of the charge density at $q^M \geq 0$, all plots are linear over a large range of charge densities and approximately parallel to each other (Fig. 4(B)). The inset represents the Γ_c versus q^M curves for 1 mM bromide adsorbed at the three substrates Ag(100), Au(111) and Hg [64–66]. The shapes of these curves are rather similar, which indicate comparable values of the Esin–Markov coefficient $-(\partial\Gamma/\partial q^M)_c$ for bromide adsorption on the three metals. The shift of the three curves with respect to each other reveals that bromide adsorption is somewhat stronger on gold, in comparison to silver and mercury, e.g. Au(111) > Ag(100) > Hg. This sequence agrees well with the results of a recent quantum chemical cluster calculation on the adsorption of halide ions on noble metals [67]. In addition we note that the adsorption strength of halide and oxyions on the low-index faces of silver was found to increase in the following order: Ag(110) < Ag(100) < Ag(111) [6,27,28,68].

3.2.3. Electrosorption valency and Esin–Markov plot

The electrosorption valency [66], or, in other words, the charge number at constant electrode potential [10], is determined from a plot of the charge density versus surface excess at constant potential. Independently, γ' is obtained from the first derivative of the zero coverage Gibbs energy of adsorption ($\theta_c \rightarrow 0$), ΔG_{ads}, versus E (Fig. 10, see below):

$$\gamma' = \frac{1}{F}\left(\frac{\partial \Delta G_{ads}}{\partial E}\right)_{\Gamma c} = -\frac{1}{F}\left(\frac{\partial q^M}{\partial \Gamma_c}\right)_E \tag{2}$$

Fig. 6 shows a series of q^M versus Γ_c-data of selected electrode potentials. The plots are fairly linear. The corresponding values of γ' are plotted in Fig. 7 (filled circles). These results are in agreement with γ' as obtained from the first derivative of ΔG with respect to E (dotted line). γ' seems to decrease slightly with increasing electrode potential and approaches, for instance, values of $-(0.80 \pm 0.05)$ at $E = -0.500$ V. This result is comparable with recently reported data for Br^-/Au(111) [65], but significantly smaller than the results for Br^-/Hg ($\gamma' \sim -0.34$) [66].

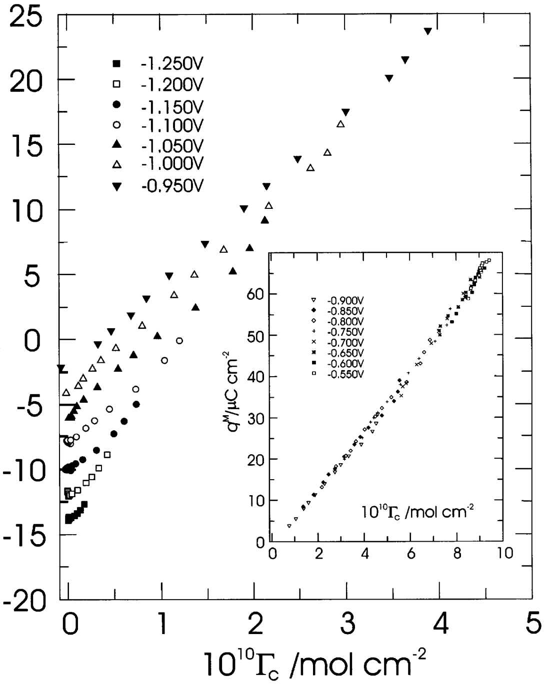

Fig. 6. Electrode charge density versus Gibbs surface excess at constant potential. The inset shows the entire coverage region.

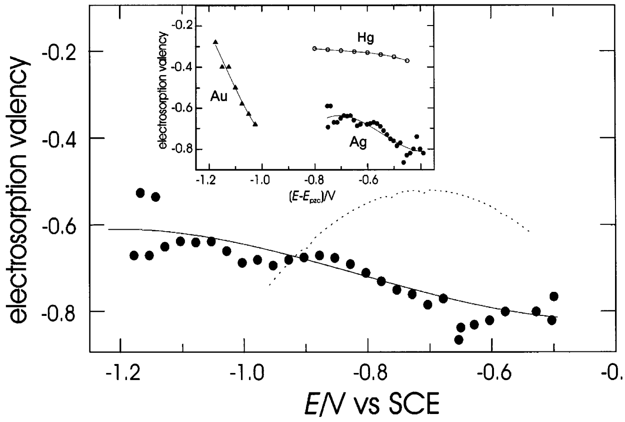

Fig. 7. Electrosorption valency γ' versus potential computed from the slopes of q^M versus Γ (○) and ΔG_{ads} versus E (dotted line). The inset shows the potential dependence (rational scale) of the electrosorption valencies of bromide adsorbed on mercury [66] and on Au(100).

In addition, the first derivative of the electrode potential with respect to the chemical potential of the adsorbate at constant charge, the so-called Esin–Markov coefficient (which is the reciprocal number of electrons flowing to the interface per adsorbed bromide at constant chemical potential [10]), should be equal to $\partial\Gamma_c/\partial q^M$ [2]:

$$\frac{1}{RT}\left(\frac{\partial E}{\partial \ln c_{Br^-}}\right)_{q^M} = -\left(\frac{\partial \Gamma_c}{\partial q^M}\right)_{\ln c_{Br^-}} \tag{3}$$

E versus $-RT \ln c_{Br^-}$ is plotted in Fig. 8A at various charges ranging between -10 and 62 μC cm^{-2}. Except at the most negative charge density all correlations are fairly linear, as indicated by the dashed lines. The corresponding slopes yield directly the Esin–Markov coefficients. These data agree well with $-(\partial\Gamma_c/\partial q^M)_{\ln c_{Br^-}}$ (cf. Fig. 4(B) and Fig. 8(B)). The linear dependences also enable us to estimate a rather singular value -0.85 ± 0.05 for the charge number at constant chemical potential $n' = -1/F(\partial q^M/\partial\Gamma_c)_{\ln c_{Br^-}}$. The corresponding result for bromide on Au(111) amounts to -0.97 [65].

Furthermore, we note that both data sets referring to the cross-relations expressed by Eqs. (2) and (3) demonstrate convincingly that the thermodynamic analysis of our chronocoulometric data is throughout self-consistent.

3.2.4. Energetics of adsorption

Employing the results discussed above we present in the following paragraph an attempt to extract information on the energetics of adsorbate–substrate and lateral adsorbate–adsorbate interactions. The analysis of our experimental data is based (i) on the empirical virial-type isotherm within the zero-coverage limit [6,69] and (ii) on a lattice gas model taking into account the local adsorption at finite coverages [35–37,50].

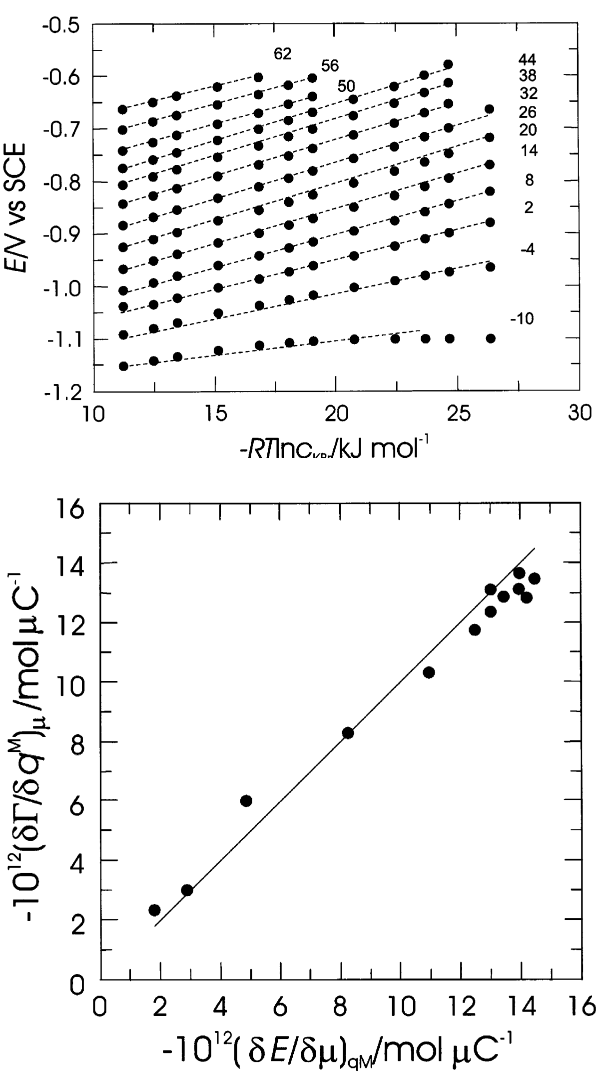

Fig. 8. (A) Esin–Markov plots. (B) comparison of the Esin–Markov coefficients determined from the slope of E versus μ (Fig. 10(A)) or by differentiation of Γ versus q^M (Fig. 4(B)).

3.2.5. Low coverage limit

To determine the Gibbs energy of adsorption we followed Parsons' suggestion for ionic systems and fitted the equation of the empirical square-root-isotherm (4) to the surface pressure data [6,69].

$$\ln\,(k_BTc_{Br}) + \ln\,\beta = \ln\,\Phi + B\Phi^{1/2} \tag{4}$$

where $\beta = \exp(-\Delta G_{ads}/k_BT)$ is the adsorption equilibrium constant at zero coverage, B is a constant and $\Phi = (\xi_o - \xi)_{q^M}$ the surface pressure. When the analysis was carried out at constant potential, Φ was substituted by the film pressure $\pi = (\gamma_o - \gamma)_E$ [7]. We also note that Eq. (4) reduces at low coverages to Henry's law $\Phi = k_BT\beta c$. Fig. 9(A) and Fig. 9(B) show plots of $\pi^{1/2}$ versus $\ln\,(k_BTc_{Br}/\pi)$ at constant potential and $\Phi^{1/2}$ versus $\ln\,(k_BTc_{Br}/\Phi)$ at constant charge density. Both data sets are fairly linear and allow therefore the extrapolation to zero film and surface pressure, respectively. The intercepts with the abscissa yield $-\ln\beta$, from which the Gibbs energies of adsorption can be calculated. The results are plotted in Fig. 10. The standard state is an ideal $\Gamma = 1$ ion cm^{-2} for the adsorbed species and an ideal $c_{Br} = 1$ mol dm^{-3} for the bulk species. Both plots, ΔG_{ads} versus E and ΔG_{ads} versus q^M, are non-linear, which reflects the multistate character of bromide adsorption on Ag(100). Non-linear dependences were also reported for SO_4^{2-}, Cl^- and Br^- adsorbed on an Au(111) electrode [7–10,62].

Unfortunately, Eq. (4) lacks a real physical basis and should be primarily considered as a convenient method for linearising experimental data to determine the Gibbs energy of adsorption in the zero coverage limit. Attempts to incorporate structural information and to explore the nature of lateral interactions require the analysis of complete Γ versus c (or E) isotherms.

3.2.6. Finite coverage limit

The adsorption of bromide ions on Ag(100) is described by a (square) lattice-gas model employing the grand-canonical Hamiltonian of the form

$$H = \varepsilon_{ij}\sum_{ij} c_i c_j - \mu \sum_{i} c_i \tag{5}$$

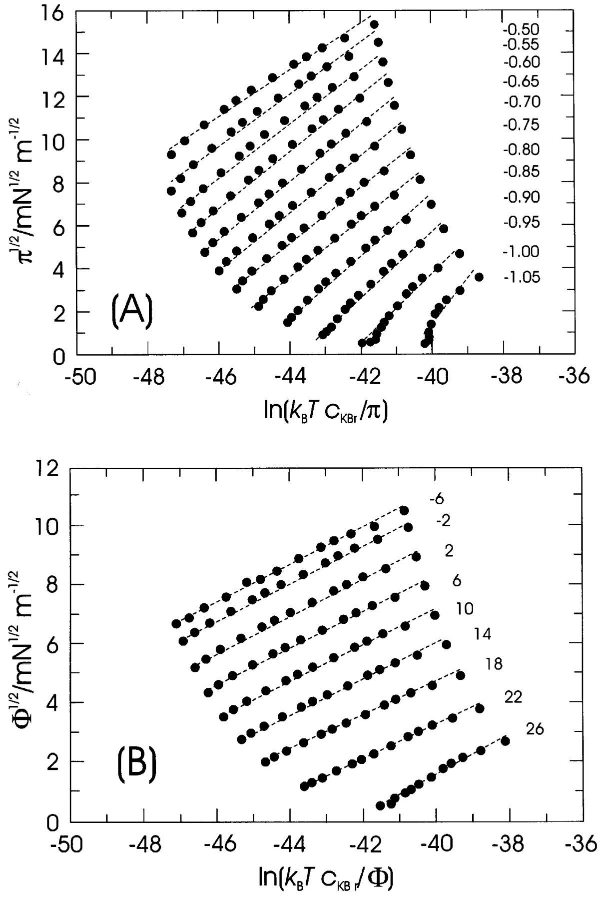

Fig. 9. Fit of the adsorption data to the equation of the square root isotherm at constant potential (A) and constant charge density (B).

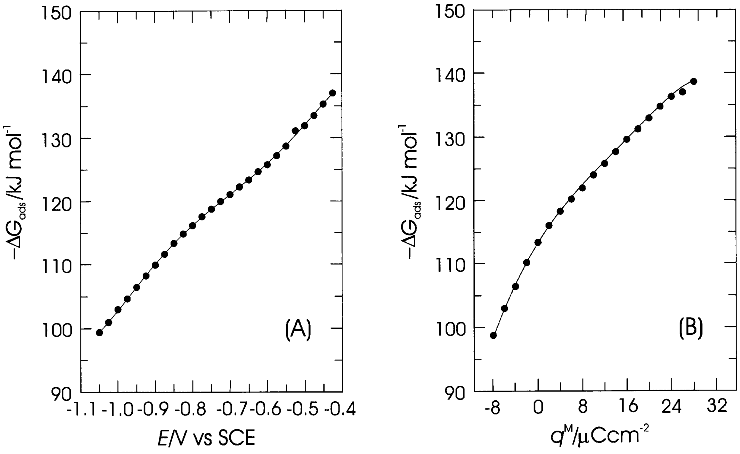

Fig. 10. Plots of the Gibbs energy of bromide adsorption on Ag(100) as determined with the square root isotherm (Eq. (4)) at constant electrode potential (A) and constant charge density (B).

where c_i is either 1 or 0 depending on whether site i is occupied or not, ε_{ij} is the lateral interaction energy between two species on sites i and j, μ is the (electro)chemical potential of the ion and the sums Σ_i and Σ_{ij} run over all sites and pairs of sites, respectively [70].

The surface coverage of the adsorbed ion, which is a function of the electrochemical potential μ, is given by

$$\theta = N^{-1}\sum_i c_i \qquad (6)$$

N is the total number of the surface sites on the lattice, e.g. θ refers to the number of silver atoms of the Ag(100) − (1 × 1) surface.

The relation between the electrochemical potential μ, the single particle adsorption energy ε_{ads} (the sign convention of ε_{ads} is such that ε_{ads} is positive when a particle is removed from the bulk solution and adsorbed on the surface) at a chosen reference potential (here the potential of zero charge, E_{pzc}), the halide bulk concentration c and the electrode potential E is given by [35,36]

$$\mu = \varepsilon_{ads} + k_B T \ln c - e_o \gamma'(E - E_{pzc}) \qquad (7)$$

where e_o is the elementary charge.

Based on the above model, two approaches were tested to describe quantitatively the experimental θ_c versus E isotherms of bromide adsorption on Ag(100) (Fig. 11).

3.2.6.1. Modified quasi-chemical approximation (QCA) [35,36]. This model represents an approximate analytical theory for the surface coverage as a function of the electrochemical potential. Nearest neighbours will be treated exactly while all other interactions, including those between nearest neighbours with their neighbours are treated within the mean field approximation. Lateral interactions are considered as the sum of long-range electrostatic interactions, ε_{elec}, and a short-range non-electrostatic interaction, ε_{nn}, that is restricted to

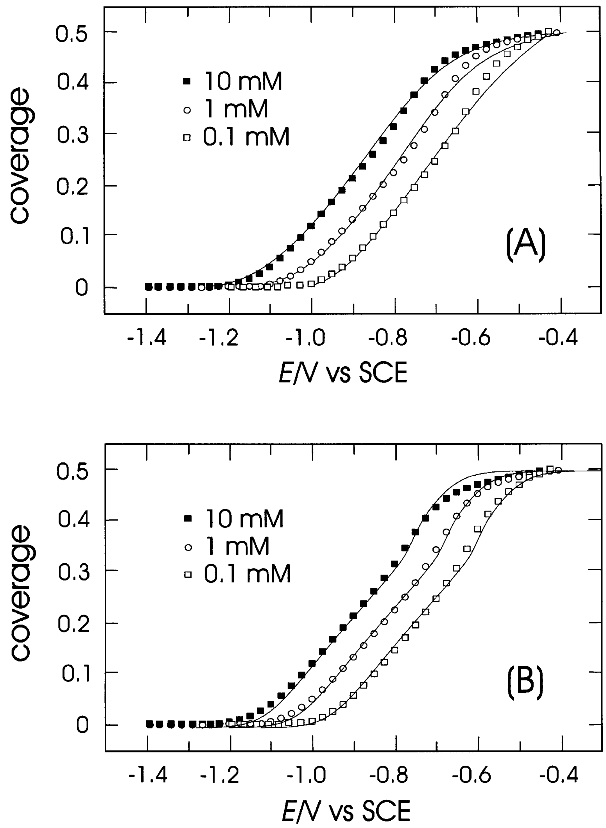

Fig. 11. Potential dependence of the chronocoulometrically determined coverage θ_c (referenced to the Ag(100) − (1 × 1) lattice) for three KBr concentrations in (0.05 − x) M KClO$_4$ on Ag(100). The solid lines in Fig. 11(A) were determined by fitting the experimental data to the isotherm based on the modified QCA [31]. The corresponding parameters for $\varepsilon_{ads} + kT\ln c$, ε_{nn}, ε_{elec} and $\gamma' = A + B\ E$ (Eqs. (5) and (6)) are summarised in Table 1. The solid lines in Fig. 11(B) represent the Monte-Carlo-simulation isotherms as calculated by Rikvold and co-workers [50]. For further details see text.

Table 1
Results of the fit of Eqs. (5) and (6) with the assumption of a linear potential dependence of γ' to the experimental θ versus E-isotherms (cf. also Fig. 11)

c/mM	ε_{nn}/eV	ε_{elec}/eV	$(\varepsilon_{ads}+kT\ln(c))$/eV	A	B/V	r^2
0.1	−0.039	0.150	0.01825	−1.3	−0.453	0.993
1.0	0.0272	0.107	−0.0338	−1.2	−0.464	0.995
10	0.0878	0.093	−0.090	−1.2	−0.444	0.9979

nearest neighbours. ε_{elec} accounts for the lateral surface dipole interaction between two ions R apart, modified by screening of the electrolyte: $\varepsilon_{elec}=2\mu_s^2/(R\varepsilon_s)(1+\kappa R)\exp(-\kappa R)$, $1/\kappa$ is the well-known dielectric screening length and ε_s is the static dielectric constant. The model accounts for the following structural information of the SXS-measurements: (1) square symmetry of the substrate surface, (2) localised adsorption of bromide, (3) the formation of an ordered c(2 × 2) adlayer at saturation coverage $\theta=0.5$.

Based on the modified QCA Koper obtained the following expression for μ [35,36]

$$\mu=2\varepsilon_{nn}^{eff}+3.784\theta\varepsilon_{elec}+k_BT\ \ln\left(\left(\frac{1-\theta}{\theta}\right)\left(\frac{\beta_{eff}-1+2\theta}{\beta_{eff}+1-2\theta}\right)^2\right) \tag{8}$$

with the effective nearest neighbour interaction

$$\varepsilon_{nn}^{eff}=\varepsilon_{nn}+0.9804\varepsilon_{elec} \tag{9}$$

and

$$\beta^{eff}=(1-4\theta(1-\theta)(1-\exp(-\varepsilon_{nn}^{eff}/k_BT)))^{1/2} \tag{10}$$

The expression for ε_{nn}^{eff} represents the contribution of non-electrostatic and electrostatic interactions to the nearest neighbour interaction energy. Modelling the remaining non-nearest neighbours (electrostatic) interactions within the mean field approximation gives the term $3.784\varepsilon_{elec}\theta$. The complete derivation is described in Refs. [35,36].

The combination of Eq. (7) and Eq. (8) allows us to fit the experimental θ_c versus E-isotherms, employing initially ε_{nn}, ε_{elec} and ε_{ads} as adjustable parameters. E_{pzc} was fixed at −0.885 V. Fine tuning showed that the best fit of the above model to the experimental chronocoulometric data was obtained by allowing the electrosorption valency γ' to vary linearly with the electrode potential, e.g. $\gamma'=A+BE$ (Fig. 11(A), Table 1, cf. also Ref. [47]). The following results were obtained:

1. The modified QCA accounts for the local order of bromide adsorption on Ag(100) and allows us to model the plateau of the experimental θ_c versus E isotherm, occurring at $\theta_c=0.5$ due to the formation of the long-range ordered c(2 × 2) adlayer. This is a significant improvement with respect to the mean field (Frumkin) model, which assumes complete disorder at all coverages.
2. The dominant interactions are repulsive long range electrostatic interactions, combined with an additional short range repulsion when two neighbouring sites are apparently occupied. From the electrostatic interaction energy ε_{elec} ranging between 150 meV (0.1 mM KBr) and 93 meV (10 mM KBr) an apparent surface dipole moment of the adsorbed bromide ions was estimated as 0.38 D < μ_s < 0.48 D (cf. Table 1). Here, the value of the vacuum dielectric constant was chosen for ε_s.
3. The contribution due to short range repulsion seems to decrease with decreasing bromide concentration. This observation might suggest that the lateral interaction energies ε_{ii} are not entirely potential independent, as is assumed in the present model.
4. The relation between the single ion adsorption energy ε_{ads} and the standard Gibbs adsorption energy ΔG_{ads}, the quantity obtained from the thermodynamic analysis in the low coverage limit (cf. square root isotherm [69]) is given by

$$\Delta G_{ads}=\varepsilon_{ads}+k_BT\ \ln\left(\frac{\Gamma_s}{lc_s}\right) \tag{11}$$

   Here, Γ_s represents the number of particles in the adsorbed standard state (1 cm^{-2}), c_s is the number of particles in the bulk standard state (1 mol dm^{-3}) and l is the thickness of the double layer, here assumed to be approximately 3 Å. The fits of the isotherm based on the modified QCA (Eqs. (7) and (8)) to our experimental θ versus E isotherms give values of ΔG_{ads} at E_{pzc} of about −95 kJ mol^{-1}. This result compares with −109 kJ mol^{-1} when using the Parsons analysis (Fig. 10). The agreement is satisfactory.
5. The modified QCA does not allow us to reproduce the experimentally observed inflection point of the isotherms around $\theta_c\approx0.37$ (indicating the onset of the formation of long-range ordered patches of the c(2 × 2) adlayer). Modelling of this phase transition requires the exact treatment of higher order neighbours, as shown in two recent MC-studies [35,36,50].

3.2.6.2. Monte Carlo simulations [35,36,50]. Koper performed the first equilibrium Monte Carlo simulation for bromide on Ag(100) with the above lattice gas model exploring the role of finite or infinite nearest-neighbour repulsion and screened dipole–dipole interactions [35,36]. The results of this study motivated recently a rather comprehensive investigation of Rikvold and co-workers [50]. These authors found that the lateral interactions are quite adequately described with a nearest-neighbour excluded volume interaction (infinite nearest-neighbour repulsion, cf. also Ref. [47]) related to the large radius of Br (1.96 Å [71]), plus a long range dipole–dipole repulsion. The following set of pairwise interactions was used in their work: $\varepsilon(R) = -\infty$ $(R = 1)$; $\varepsilon(R) = 2^{2/3}\ \varepsilon_{\mathrm{nnn}}/R^3$ $(\sqrt{2} \le R \le 5)$ and 0 at $R > 5$ (truncation), where R is the separation of an interacting bromide pair within the adlayer and $\varepsilon_{\mathrm{nnn}}$ is the lateral dipole–dipole repulsion between next-nearest neighbours. Rikvold and co-workers applied a non-linear fitting method to compare the simulated $\theta(\mu)$ (cf. Eqs. (5)–(7), grid size $L = 32$ or $L = 128$, room temperature (r.t.)) with the experimental θ_c versus E isotherms obtained from chronocoulometry. When choosing an arbitrary reference level for the electrochemical potential, instead of E_{pzc} in Eq. (5), the authors obtained the following resulting parameter values: $\varepsilon_{\mathrm{nnn}} = (26 \pm 2)$ meV and the electrosorption valency $\gamma' = -(0.73 \pm 0.03)$ [50]. These results are consistent with previous analytical approaches (see Section 3.2.4 as well as Refs. [35,47]). The fitted MC-isotherms are plotted together with the chronocoulometric isotherm in Fig. 11(B). The agreement for the two lowest concentrations is excellent, while the agreement is somewhat less satisfactory for the highest concentrations. The isotherms show a long gradual slope in the disordered phase. At critical electrochemical potentials of the second order phase transitions between the low-coverage disordered phase and the c(2 × 2) ordered phase the coverage amounts to 0.37 ± 0.01. These results coincide excellently with the chronocoulometric isotherms, and are within statistical errors the same as the critical coverage for the pure hard-square model [62].

3.3. Model of the inner layer

Many models have been developed to describe the structure of the metal | electrolyte interface in the presence of specifically adsorbed anions (a recent review is given in Ref. [72]. Most of the data obtained on mercury and on solid electrodes were analysed using the Grahame–Parsons model of the Helmholtz layer [73,74]. The basic assumptions of this approach are: (i) a total separation of charge at the interface, (ii) a specific vertical location of adsorbed species (inner Helmholtz-plane) and (iii) the inner layer is treated as a dielectric continuum. This model of the interface does not contain any lateral inhomogeneities of the electrode surface. These assumptions are rather severe; some of their inadequacies have been pointed out recently [72]. Despite this criticism we will employ the Grahame–Parsons model in our discussion to (i) complement our structural data and thermodynamic quantities of bromide adsorption and (ii) to compare our results with other studies.

The Helmholtz-capacity C_{H} was calculated from the total equilibrium electrode capacity determined by differentiation of the q^{M} versus E-curves (cf. Figs. 2 and 3) according to [6]:

$$C_{\mathrm{H}}^{-1} = C^{-1} - C_{\mathrm{d}}^{-1}\left(1 + zF\frac{\partial \Gamma_{\mathrm{Br}}}{\partial q^{\mathrm{M}}}\right) \tag{12}$$

C_{d} is the capacitance of the diffuse layer. The gradient $(\delta\Gamma_{\mathrm{Br}}/\delta q^{\mathrm{M}})$ is the Esin–Markov coefficient and was computed with the data of Fig. 4(B). The Helmholtz-capacity C_{H} is plotted as a function of the electrode charge density in Fig. 12. C_{H} seems to be rather independent of the bulk bromide concentration and practically coincides with the experimental equilibrium capacity of the higher concentrated bromide solutions $(c \ge 10^{-3}$ M) $C = \partial q^{\mathrm{M}}/\partial E$ (solid line in Fig. 12). The main effect of the second term in Eq. (12) is obviously to suppress the contribution of the diffuse layer. The C_{H} versus q^{M}-plots exhibit one minimum and two maxima: one is rather close to $q^{\mathrm{M}} = 0$, actually at the same position but with a somewhat higher magnitude than reported for Ag(100)/(x M $KClO_4$ + (0.02 − x) M KPF_6) [23] (dashed line Fig. 12). The similarities between these two data sets point to a contribution in C_{H} due to the reorientation of interfacial water molecules in this region. This hypothesis is supported by the results of a recent ATR–FTIR study at the interface

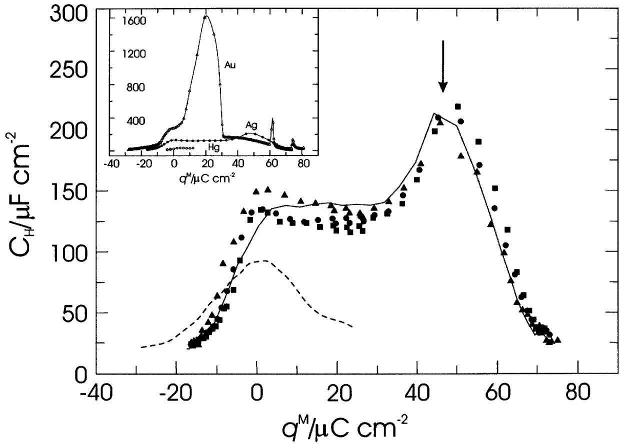

Fig. 12. Helmholtz of the Ag(100) electrode in (0.05 − x) M $KClO_4$ + x M KBr: (■) 2×10^{-4} M; (○) 10^{-3} M, (▲) 10^{-2} M. The solid line represents the experimental capacitance for 10^{-3} M KBr in 0.049 M $KClO_4$ as obtained by differentiation of the chronocoulometrically measured charge density q^{M} versus the electrode potential. The dashed curve is the Helmholtz capacity of Ag(100) in 0.01 M KPF_6 + 0.01 M KF [23]. The inset compares the Helmholtz capacities for the bromide adsorption on Ag(100) with corresponding data on mercury [64] and Au(100) [44].

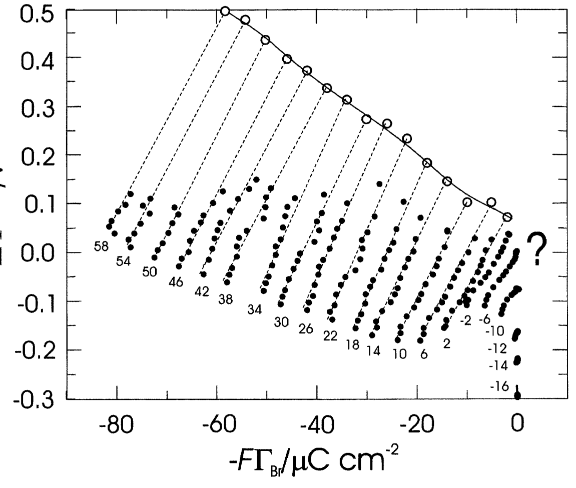

Fig. 13. Change in the potential drop across the inner layer, $\Delta\phi^{M-2}$, of an Ag(100) electrode as a function of the adsorbed amount of bromide (expressed as $-F\Gamma$) at constant charge density on the metal side of the interface. The open circles represent $\Delta\phi^{M-2}$ at the condition of zero diffuse layer charge (The data below 2 μC cm^{-2} (solid points) are shown to illustrate our experimental findings in this study. Because of their lower accuracy they are not included in any quantitative analysis).

between various aqueous electrolytes and thin silver films [75]. The second maximum occurs at $q^M \sim 47$ μC cm^{-2}, which agrees fairly well with the position of the lattice-gas → c(2 × 2) adlayer transition. Therefore it is clearly associated with properties of the bromide adlayer.

The Helmholtz-capacity C_H is a function of two variables, the charge on the metal and the amount of adsorbed anions. Therefore, it may be expressed in terms of two components, the capacitance at constant amount adsorbed, ${}_{q^M}C$, and the capacitance at constant electrode charge density, ${}_{\Gamma}C$ [6,73,74]:

$$C_H^{-1} = {}_{q^M}C^{-1} + zF\left(\frac{\partial\Gamma_{Br^-}}{\partial q^M}\right)_{\Gamma C^{-1}} \qquad (13)$$

The quantity ${}_{\Gamma}C$ is estimated from the first derivative of the potential drop across the Helmholtz-layer $\Delta\phi^{M-2} = E - E_{pzc} - \phi^2$ versus the charge $zF\Gamma_{Br^-}$ ($z = -1$) of adsorbed bromide at constant electrode charge density q^M. ϕ^2 is the potential drop across the diffuse layer. The $\Delta\phi^{M-2}$ versus $-F\Gamma$-data, as shown in Fig. 13, are fairly linear. Consequently, ${}_{\Gamma}C$ may be understood as an integral capacity. Scatter was observed only in the low concentration region ($c \leq 5 \times 10^{-5}$ M KBr). These data were not considered in the regression analysis.

Next, the capacity at constant amount adsorbed ${}_{q^M}C$, was computed by inserting the previously determined values of C_H, ${}_{\Gamma}C$ and $(\partial\Gamma_{Br^-}/\partial q^M)$ (Fig. 4(B)) into Eq. (13). ${}_{q^M}C$ was also calculated using the data shown in Fig. 13 and calculating the first derivative of q^M versus $\Delta\phi^{M-2}$ at Γ_{Br^-} = constant (open circles in Fig. 14(A)). Both approaches yield similar results. The dependences of ${}_{\Gamma}C$ and ${}_{q^M}C$ on the electrode charge density are plotted in Fig. 14. The curves are non-linear. Both exhibit maxima around −(2 to 5) μC cm^{-2}, which correspond to the potential region of the broad capacitance maximum in Fig. 1. We also notice, that around $q^M \approx 0$ the capacity at constant amount adsorbed, ${}_{q^M}C$, is significantly smaller for Br$^-$/Ag(100) than for electrolytes containing only slightly specifically adsorbed ions like KPF$_6$ or KClO$_4$ (dashed line in Fig. 14(A)). This provides evidence for interactions between water molecules and bromide ions even at rather low coverages, and implies that P1 is not exclusively caused by reorientation of water molecules. At small positive charge densities ${}_{\Gamma}C$ and ${}_{q^M}C$ initially decrease and then seem to approach rather adsorbate–concentration inde-

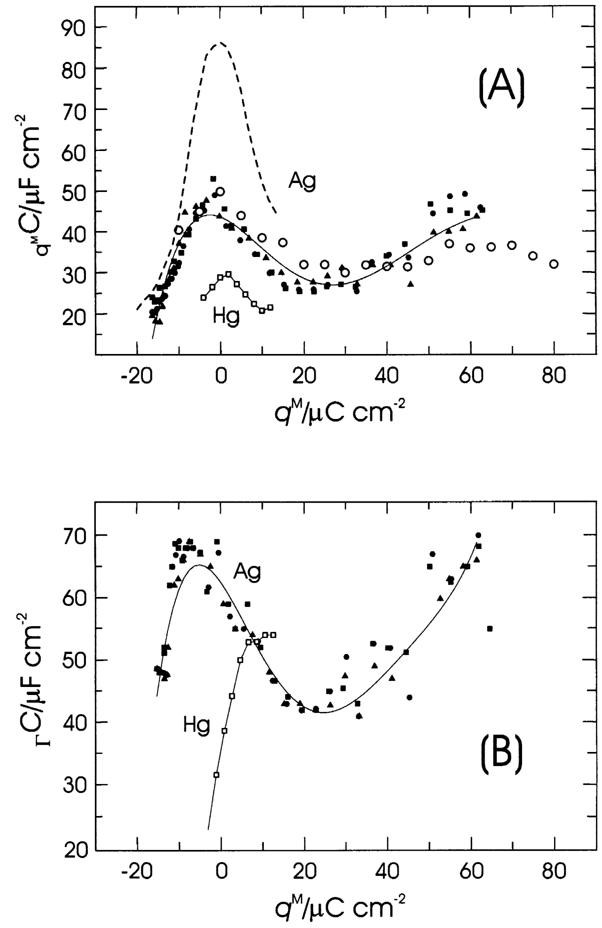

Fig. 14. Components of the Helmholtz capacity on Ag(100) in the presence of bromide ions at constant amount adsorbed (A) and at constant charge density (B) as calculated with Eq. (13). The full symbols represent the following bromide concentrations (M): (■) 2 × 10^{-4}, (○) 10^{-3}, (▲) 10^{-2}. The ${}_{q^M}C$ versus q^M curve symbolised by the open circles in (A) was computed from the slopes of $\Delta\phi^{M-2}$ versus q^M at Γ_{Br^-} = constant. For comparison, the components of the Helmholtz capacity for bromide adsorbed on mercury [64] as well as the Helmholtz capacity at constant amount adsorbed for 0.01 M KPF$_6$ + 0.01 M KF on Ag(100) ([23], dashed line) were added.

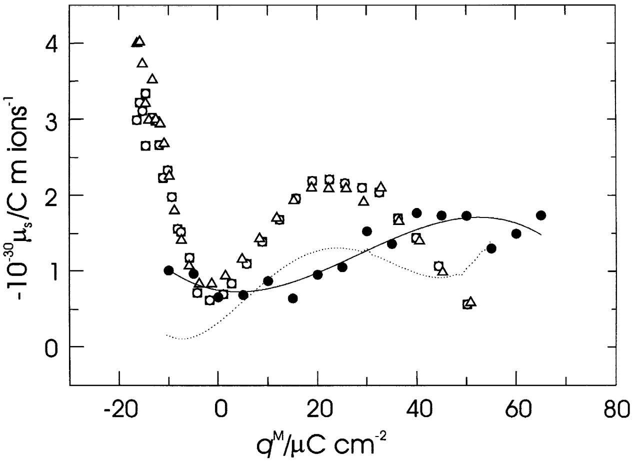

Fig. 15. Plots of the effective dipole moment formed by bromide on Ag(100) versus the electrode charge density. The individual symbols represent μ_s as determined from the values of the electrosorption valency (Eqs. (13) and (16)) for three bromide concentrations (□ 2×10^{-4} M, ○ 10^{-3} M, ▲ 10^{-2} M). $_{q^M}C$ in Eq. (13) was either determined with Eq. (13) (open symbols) or through $\partial(-F\Gamma)/\partial(\Delta\phi^{M-2})$ at constant amount adsorbed (*l*). The dotted line was calculated from the $\Delta\phi^{M-2}$ versus $-F\Gamma$ plot under conditions of zero diffuse layer charge.

pendent values, (43 ± 5) µF cm^{-2} and (27 ± 4) µF cm^{-2} in 10 µC cm^{-2} < q^M < 50 µC cm^{-2}, respectively. Unfortunately, the low precision of the experimental data at q^M > 50 µC cm^{-2} does not allow us to determine any reliable trends at more positive charge densities. But we should recall that the majority of adsorbed bromide ions are situated in fourfold hollow sites of the substrate lattice and incorporated into the ordered c(2 × 2) overlayer at q^M > 47 µC cm^{-2} (cf. Figs. 1–4).

The capacities at constant charge and constant amount adsorbed may be considered as integral quantities described by [26,73,74]:

$$_{\Gamma}C = \varepsilon/(x_2 - x_1) \tag{14a}$$

$$_{q^M}C = \varepsilon/x_2 \tag{14b}$$

where x_2 and x_1 are the distances of the outer and the inner Helmholtz planes from the metal surface, and ε is the permittivity, respectively. In terms of this model the detailed interpretation of the $_{\Gamma}C$ versus q^M-curves is still rather difficult since they are affected by both the change of the permittivity as well as the position of the inner Helmholtz plane x_1. The analysis of the $_{q^M}C$ is more straightforward because one might assume, at constant amount adsorbed, that the thickness of the inner layer x_2 does not change with charge (cf. Eq.(14b)). Therefore, the shape of $_{q^M}C$ versus q^M should reflect the change of the inner layer permittivity with the charge on the metal. The change of the inner layer permittivity is correlated to the orientation of water dipoles at the electrode surface as well as their ability to screen adsorbed anions. Due to the dielectric saturation the permittivity is expected to be low at very positive and very negative fields, and to display a maximum at small charge densities, where solvent molecules reorient and their disorientation is at a maximum. This scenario is found for non- or only slightly specifically adsorbed anions, such as PF_6^- and/or F^- on Ag(100) (dashed curve in Fig. 14(A)). The presence of specifically adsorbed bromide ions changes this pattern remarkably. Similarly as in the case of halide ion adsorption on Au(111) [75] dramatic changes of the water structure on Ag(100) are expected. Correlations between the charge (potential-) dependent interfacial water structure, as studied with ATR–FTIR [75,76] and $_{q^M}C$ (eventually $_{\Gamma}C$) offer a fascinating opportunity to test the validity of the Grahame–Parsons model of the inner layer capacitance, and, in consequence, to improve it.

The contribution of the metal to the Helmholtz capacity is also not negligible [72]. This is reflected by comparison of the Helmholtz capacity C_H and its components $_{\Gamma}C$ and $_{q^M}C$ for Ag(100), Au(111) or Hg-electrodes in the presence of bromide. The following relations were found [64,65]:

1. C_H for Au(111) is much higher within the entire accessible charge density range than the values for Ag(100) and Hg.
2. the magnitudes of $_{\Gamma}C$ and $_{q^M}C$ are similar for silver, gold and mercury, but they still follow a systematic trend: Au(111) ≥ Ag(100) > Hg. The data for Au(100) are not yet available.

The ratio of the Helmholtz-capacities at constant amount adsorbed and at constant charge densities gives the electrosorption valency [26]

$$\gamma' = z\left(\frac{_{q^M}C}{_{\Gamma}C}\right) \tag{15}$$

where $z = -1$ is the free charge of the bromide ion. This value may be used to calculate an effective surface dipole moment μ_s (open symbols in Fig. 15), which represents the dipole formed between the adsorbed adion and its image charge in the metal [26,27,77]:

$$\mu_s = \frac{ze_o\varepsilon(1-\gamma'/z)}{_{q^M}C} \tag{16}$$

ε stands for the permitivity of the Helmholtz-layer and was set equal to $\varepsilon_o = 8.85\times10^{-12}$ C^2 J^{-1} m^{-1} as suggested in Ref. [26]. Alternatively, μ_s was determined from the data shown in Fig. 13. The plots of the potential drop across the Helmholtz-layer, $\Delta\phi^{M-2}$, versus the amount of adsorbed species (here expressed as the specifically adsorbed charge $-F\Gamma_{Br^-}$) at constant electrode charge q^M were extrapolated to the points, where $q^M = F\Gamma_{Br^-}$ (open circles in Fig. 13). Under these conditions no diffuse layer exists and the potential drop $\Delta\phi^{M-2}$ is equal to the total potential drop across the interphase. The accuracy of the experimental data in Fig. 13 allowed satisfactorily linear extrapolation according to this procedure for $-10\ \mu\text{C cm}^{-2} < q^{\text{M}} < 54\ \mu\text{C cm}^{-2}$. These results demonstrate that the potential drop across the interface increases with bromide adsorption, which is equivalent to an increase of the work function. The same trend was also reported for Br^-/Ag(110) [26] and Ag(111) [27,28] as well as for SO_4^{2-}/Au(111) [7], Cl^-/Au(111) [9] and Br^-/Au(111) [65]. Differentiation of the plot of the extrapolated values of $\Delta\phi^{\text{M}-2}$ versus the amount adsorbed, Γ, yields finally the surface dipole moment μ_{s} (full dots in Fig. 15) according to the Helmholtz formula:

$$\Delta\phi^{\text{M}-2} = -\frac{\Gamma\mu_{\text{s}}}{\varepsilon} \tag{17}$$

The effective surface dipole moments as determined with the two methods are in fairly good agreement. The high values of μ_{s} at negative charge densities indicate a high polarity of the substrate–adsorbate chemisorption bond. With less negative charge densities μ_{s} drops and reaches a minimum around $-(5 \pm 3)\ \mu\text{C cm}^{-2}$. The latter is followed by a subsequent slight increase in μ_{s}, which gives rise to a more (μ_{s} as calculated from values of the electrosorption valency) or less (data from $\Delta\phi^{\text{M}-2}$ versus $-F\Gamma_{\text{Br}^-}$) developed broad maximum and finally, at $q^{\text{M}} > 50\ \mu\text{C cm}^{-2}$ and within the accuracy of our measurements, μ_{s} seems to approach a constant value of $(1.2 \pm 0.5) \times 10^{-30}$ C m ions (equivalent to -0.36 D). The shape of the μ_{s} versus q^{M} graph follows closely the charge dependence of the reciprocal Helmholtz-capacity at constant amount adsorbed. We would also like to point out that the values of the apparent surface dipole moment μ_{s} as estimated from the analysis of the finite coverage isotherm in Section 3.2.6.1 is of similar magnitude.

The absolute values $|\mu_{\text{s}}|$ of the adsorbate dipole are substantially smaller then $e_{\text{o}}r_{\text{i}}$, which one would expect for the adsorption of an ion of radius r_{i} with $|z| = 1$ on a perfect conductor in a medium having a relative dielectric constant $\varepsilon_{\text{r}} = 1$. This implies that the charge of the adsorbed bromide ions is strongly screened. Similar observations were also reported for Br^-/Ag(110) [26], Br^-/Ag(111) [27,28] and several specifically adsorbed ions on Au(111) [7,8,65].

Schmickler and Guidelli showed, by representing the metal electrode with a jellium and the solution as an ensemble of hard sphere ions and dipoles, that the screening involves contributions of the metal (spill-over of electrons) as well as of the solvent (opposite orientations of the solvent molecules with respect to that of the adsorbate dipole) [77,78]. Based on these data the theoretical value of the surface dipole moment of bromide ions adsorbed on a silver electrode at $q^{\text{M}} = 0$ is predicted to be zero, which is in agreement with our experimental result of $-(0.5 \pm 0.3) \times 10^{-30}$ C m ion ($\sim -(0.15 \pm 0.08)$ D). In order to explain the charge dependence of μ_{s}, as plotted in Fig. 15, we suggest the following scenario: at negative charge densities the surface coverage of bromide on Ag(100) is very low and the solvent molecules are primarily oriented by the external electric field. Approaching $q^{\text{M}} = 0$ this field decreases and the solvent molecules residing in the Helmholtz layer will be primarily oriented by the local field of the adsorbed ions, which is equivalent to an increase of the solvent-attributed screening of the adsorbate dipole. In consequence μ_{s} decreases. With increasing bromide coverage, which parallels the increase of the electrode charge density, the solvation spheres of the bromide ions begin to overlap. This process reduces the screening by the solvent and therefore increases $|\mu_{\text{s}}|$. Simultaneously, the electrostatic adatom–adatom interaction increases and may tend to decrease $|\mu_{\text{s}}|$ by partial discharge of the adsorbate or polarisation of the adatom orbital [77–79]. And finally, approaching a state where the ordered c(2 × 2) bromide adlayer covers the entire substrate surface, μ_{s} remains constant.

The importance of the metal contribution on the adsorbate dipole and the components of the Helmholtz capacity is obvious when comparing bromide adsorption on Ag(100) with Au(111) and Hg (Figs. 12, 14 and 15). The data suggest considerable screening contributions of silver and gold, in comparison to mercury, which agrees with theoretical predictions [77].

4. Summary and conclusions

The adsorption and phase formation of bromide ions on Ag(100) have been studied with chronocoulometry and surface X-ray diffraction.

1. Bromide ions are preferentially adsorbed in fourfold hollow sites. The comparison of isotherms obtained from measurements of the X-ray intensity in the (1, 0, 0.12) position with those from chronocoulometric experiments allows the conclusion that the degree of lateral order increases with increasing coverage. With increasing electrode potential bromide undergoes a continuous phase transition from a lattice gas to an ordered c(2 × 2) adlayer.
2. Thermodynamic data of bromide adsorption, such as Gibbs surface excess, Gibbs energy of adsorption and lateral interaction energies, the electrosorption valency, Esin–Markov coefficients as well as the apparent dipole formed between the adsorbed ion and its image charge on the metal have been estimated.
3. The local order of bromide adsorption could be successfully approximated by an isotherm based on a modified quasi-chemical approximation. This approach treats nearest neighbour interactions exactly, and all other interactions with the mean field approximation. The dominant channel of lateral inter-

actions could be assigned to repulsive long-range electrostatic interactions. Depending on the adsorbate concentration, an additional contribution due to short range repulsion was found. The concentration dependence of these interactions indicates that the charge state of bromide changes somewhat with coverage and potential, which also points out some limitations of the isotherm model chosen.

4. Monte Carlo simulations by Rikvold and co-workers [50], assuming a lattice-gas model with infinite nearest-neighbour repulsion and long range dipole–dipole repulsion, represent the chronocoulometric isotherms quantitatively and provide an excellent description of the critical properties of the continuous order/disorder phase transition within the bromide adlayer on Ag(100).
5. The analysis of the adsorption isotherms in the finite coverage limit as well as the test of the Grahame–Parsons model of the Helmholtz layer allowed us to estimate the apparent surface dipole moment between a bromide ion and its image charge. The comparison of our data on Ag(100) with results for the bromide adsorption on Au(*hkl*) and Hg point to a significant dielectric screening contribution of metal and solution for Ag(100) and Au(*hkl*). Unfortunately, our estimate of μ_s is strongly model dependent. Comparison with other approaches [33,34,48] illustrates that the experimental determination and the theoretical interpretation of surface dipole moments on solid | liquid interfaces are still rather problematic. The combination of thermodynamic quantities based on our chronocoulometric experiments with systematic ATR–FTIR studies on the water structure at the aqueous electrolyte | Ag(100) interface appear to be a promising approach to develop our knowledge on the inner layer at metal | electrolyte interfaces significantly further.
6. An extension of the present work to a systematic series of halide ions on all three low-index phases of silver is highly desirable in order to understand the trends in lateral adsorbate–adsorbate and adsorbate–substrate interactions in more detail. The combination of chronocoulometric and structural data, obtained from in-situ SXS or, eventually, STM-experiments might also open a new approach to choose and/or develop proper adsorption isotherms for ionic adsorption.

Acknowledgements

Th. Wandlowski acknowledges the support of the Deutsche Forschungsgemeinschaft through a Heisenberg-Fellowship and a NATO CRG 961219. The research at Brookhaven was supported by DEO under contract DE-AC024-76CH00016. We would like to thank Professor Rikvold and his group for stimulating discussions as well as for providing the results of the MC-simulation for Ag(100)/Br prior to publication. We would also like to acknowledge enlightening discussions with Professor Otto, Dr M.T. Koper, Dr Diesing and Dr Futamara.

References

[1] D.C. Grahame, Chem. Rev. 41 (1947) 441.
[2] P. Delahay, Double Layer and Electrode Kinetics, Interscience, New York, 1965.
[3] B.B. Damaskin, O.A. Petrii, V.V. Batrakov, Adsorption organischer Verbindungen an Elektroden, Akademie-Verlag, Berlin, 1975.
[4] A. Hamelin, in: B.E. Conway, R.E. White, J.O.M. Bockris (Eds.), Modern Aspects of Electrochemistry, 1985, p. 1.
[5] J. Clavilier, R. Faure, G. Guinet, R. Durand, J. Electroanal. Chem. 107 (1980) 205.
[6] G. Valette, A. Hamelin, R. Parsons, Z. Phys. Chem. N.F. 113 (1978) 71.
[7] Z. Shi, J. Lipkowski, M. Gamboa, P. Zelenay, A. Wieckowski, J. Electroanal. Chem. 366 (1994) 317.
[8] (a) Z. Shi, J. Lipkowski, S. Mirwald, B. Pettinger; J. Electroanal. Chem. 396 (1995) 115. (b) Z. Shi, J. Lipkowski, J. Electroanal. Chem. 403 (1996) 225.
[9] A. Chen, J. Lipkowski, J. Phys. Chem. B 103 (1999) 682.
[10] J. Lipkowski, Z. Shi, A. Chen, B. Pettinger, C. Bilger, Electrochim. Acta 42 (1998) 2875.
[11] Th. Wandlowski, J.X. Wang, O.M. Magnussen, B.M. Ocko, J. Phys. Chem. 100 (1996) 10277.
[12] C. Franke, G. Piazza, D.M. Kolb, Electrochim. Acta 34 (1989) 67.
[13] R.J. Nichols, in: J. Lipkowski, P.N. Ross (Eds.), Adsorption of Organic Molecules, VCH, New York, 1992, p. 347.
[14] L.W. Leung, D. Goszola, M.J. Weaver, Langmuir 3 (1987) 45.
[15] A. Friedrich, C. Shannon, B. Pettinger, Surf. Sci. 251/252 (1991) 587.
[16] G. Richmond, in: H. Gerischer, C. Tobias (Eds.), Advances in Electrochemistry, Science and Engineering, VCH, Weinheim, 1994.
[17] D.M. Kolb, Z. Phys. Chem. N.F. 154 (1987) 179.
[18] X. Gao, G.J. Edens, F.C. Liu, A. Hamelin, M.J. Weaver, J. Phys. Chem. 98 (1994) 8086.
[19] Itaya Electrochemistry Project, Final Report No.3, 1997.
[20] M.F. Toney, J.N. Howard, J. Richer, G.L. Borges, J.G. Gordon, O.R. Melroy, D.G. Wiesler, D. Yee, L.B. Sorensen, Surf. Sci. 335 (1995) 326.
[21] B.M. Ocko, O.M. Magnussen, J.X. Wang, R.R. Adzic, Th. Wandlowski, Physica B 221 (1996) 238.
[22] G. Valette, J. Electroanal. Chem. 132 (1982) 311.
[23] G. Valette, J. Electroanal. Chem. 138 (1982) 37.
[24] G. Valette, J. Electroanal. Chem. 146 (1983) 439.
[25] G. Valette, R. Parsons, J. Electroanal. Chem. 191 (1985) 377.
[26] K. Bange, B. Straehler, J.K. Sass, R. Parsons, J. Electroanal. Chem. 229 (1987) 87.
[27] M.L. Foresti, M. Innocenti, H. Kobayashi, G. Pezzatini, G. Guidelli, J. Chem. Soc. Faraday Trans. 92 (1996) 3747.
[28] M.L. Foresti, G. Aloisi, M. Innocenti, H. Kobayashi, G. Guidelli, Surf. Sci. 335 (1995) 241.
[29] T. Vitanov, A. Popov, Trans. SAEST 10 (1975) 5.
[30] A. Popov, J. Electroanal. Chem. 384 (1995) 179.
[31] G. Beltramo, E. Santos, W. Schmickler, J. Electroanal. Chem. 447 (1998) 71.

[32] (a) C. Hahnewinkel, A. Otto, Th. Wandlowski; Surface Sci. 429 (1999) 255. (b) H. Winkes, D. Schumacher, A. Otto; Surf. Sci. 400 (1998) 44.
[33] B.M. Ocko, J.X. Wang, Th. Wandlowski, Phys. Rev. Lett. 79 (1997) 1511.
[34] B.M. Ocko, J. Wang, R. Adzic, Th. Wandlowski, Synchrotron Radiation News 11 (1998) 23.
[35] M.T.M. Koper, J. Electroanal. Chem. 450 (1998) 189.
[36] M.T.M. Koper, Electrochim. Acta 44 (1998) 1207.
[37] G. Brown, P.A. Rikvold, S.J. Mitchell, M.A. Novotney, in: A. Wieckowsky (Ed.), Interfacial Electrochemistry, Dekker, New York, 1998, p. 47.
[38] D. Dickertmann, F.D. Koppitz, J.W. Schultze, Electrochim. Acta 21 (1976) 967.
[39] A. Bewick, B. Thomas, J. Electroanal. Chem. 65 (1975) 911.
[40] M. Dietterle, PhD Thesis, University of Ulm, 1996
[41] Th. Wandlowski, M.H. Hölzle, Langmuir 12 (1996) 6597.
[42] M.L. Foresti, M. Innocenti, R. Guidelli, J. Electroanal. Chem. 376 (1994) 85.
[43] T. Pajkossy, Th. Wandlowski, D.M. Kolb, J. Electroanal. Chem. 414 (1996) 209.
[44] Th. Wandlowski, Mod. Chem. 137 (2000) 393.
[45] Z. Shi, J. Lipkowski, J. Electroanal. Chem. 369 (1994) 283.
[46] I.K. Robinson, D.J. Tweet, Rep. Progr. Phys. 55 (1992) 599.
[47] J.X. Wang, Th. Wandlowski, B.M. Ocko; Proceedings of the 191th ECS-Meeting, Montreal, 1997.
[48] D.E. Taylor, E.D. Wiliams, R.L. Park, N.C. Bartelt, T.L. Einstein, Phys. Rev. B 32 (1985) 4653.
[49] B.N.J. Person, Surf. Sci. Rep. 15 (1992) 1.
[50] S.J. Mitchell, G. Brown, P.A. Rikvold, J. Electroanal. Chem. 493 (2000) 68.
[51] O. Endo, M. Kiguchi, T. Yokoyama, M. Ito, T. Ohta, J. Electroanal. Chem. 473 (1999) 19.
[52] R.G. Linford, Chem. Rev. 78 (1978) 81.
[53] D.M. Mohilner, R. Beck, J. Phys. Chem. 83 (1979) 1160.
[54] K.E. Heusler, G. Lang, Electrochim. Acta 42 (1997) 747.
[55] T.A. Brunt, E.D. Chabala, T. Rayment, S.J. O'Shea, M.E. Welland, J. Chem. Soc. Faraday Trans. 92 (1996) 3807.
[56] J. Lipkowski, W. Schmickler, D.M. Kolb, R. Parsons, J. Electroanal. Chem. 452 (1998) 193.
[57] W. Haiss, J. Sass, J. Electroanal. Chem. 410 (1996) 119.
[58] H. Ibach, C.E. Bach, M. Giesen, A. Grossmann, Surf. Sci. 375 (1997) 107.
[59] H. Ibach, Surf. Sci. Rep. 29 (1997) 193.
[60] S. Wu, J. Lipkowksi, O.M. Magnussen, B.M. Ocko, Th. Wandlowski, J. Electroanal. Chem. 446 (1998) 67.
[61] L. Stolberg, J. Lipkowski, in: J. Lipkowski, P.N. Ross (Eds.), Adsorption of Molecules at Electrodes, VCH, New York, 1993.
[62] Z. Racz, Phys. Rev. B 21 (1980) 4012.
[63] W. Kinzel, M. Schick, Phys. Rev. B 24 (1981) 324.
[64] G.J. Hills, R.M. Reeves, J. Electroanal. Chem. 42 (1973) 355.
[65] Z. Shi, J. Lipkowksi, S. Mirwald, B. Petinger, J. Chem. Soc. Faraday Trans. 92 (1996) 3737.
[66] K.W. Schultze, K.J. Vetter, J. Electroanal. Chem. 44 (1973) 63.
[67] I. Ignaczak, J.A.N.F. Gomes, J. Electroanal. Chem. 420 (1997) 71.
[68] G. Valette, J. Electroanal. Chem. 255 (1988) 215.
[69] R. Parsons, Trans. Faraday Soc. 395 (1955) 1518.
[70] T.L. Hill, Statistical Thermodynamics, Addison–Wesley, Reading, MA, 1960.
[71] D.R. Lide (Ed.), Handbook of Chemistry and Physics, CRC Press, New York, 1999.
[72] W. Schmickler, Chem. Rev. 96 (1995) 3177.
[73] D.C. Grahame, J. Am. Chem. Soc. 80 (1958) 4201.
[74] D.C. Grahame, R. Parsons, J. Am. Chem. Soc. 83 (1961) 1291.
[75] M. Futamara, D. Diesing; personal communication.
[76] K. Ataka, M. Osawa, Langmuir 14 (1998) 951.
[77] W. Schmickler, J. Electroanal. Chem. 249 (1988) 25.
[78] W. Schmickler, R. Guidelli, J. Electroanal. Chem. 235 (1987) 387.
[79] A. Kornyshev, W. Schmickler, J. Electroanal. Chem. 202 (1986) 1.